Visualization of Time-Space Dominant Particle from CT Images Using 3D Wavelets Transform - Comparison Between Non-Choking and Pseudo Choking

Masahiro TAKEI [1], Hui LI [2], Mitsuaki OCHI [1], Yoshifuru SAITO [3]
Kiyoshi HORII [4], Tomasz DYAKOWSKI [5]

[1] Nihon University, Dept of Mech.Eng. 1-8-14 Kanda Surugadai Tokyo 101-8308 Japan,
takei@mech.cst.nih0n-u.ac.jp
[2] Kagoshima University, Kagoshima Japan, [3] Hosei University, Tokyo Japan
[4] Shirayuri College, Tokyo Japan, [5] UMIST, Manchester UK

ABSTRACT

The concept to extract dominant particle density fluctuation in various time-space frequency levels on a pipeline cross section has been launched using a capacitance-computed tomography and three-dimensional discrete wavelets transform. With this concept, particle density fluctuation at the downstream of a pipe bend is decomposed to time-space levels in a non-choking state and a pseudo choking state. As a result, this concept enables the time and position when and where particle density fluctuations with dominant time-space levels pass through the pipeline to be determined.

Keywords Capacitance CT, 3D wavelets transform, Solid air two phase flow, Particle density Fluctuation

1 INTRODUCTION

Recently, a non-invasive monitoring method of the solid behaviour with real time using computed tomography (CT) has been popular in multiphase flow measurement. Generally, CT utilise a transmitted wave such as X-ray and acoustic wave to an object to obtain the images non-invasively. The inside of the object is re-constructed from the transmitted images by a mathematical method (Rosenfeld et al. 1982). CT has been mainly developed in the medical field to visualize the inside of the human body. In a field of air-liquid two-phase flow, a high speed X-ray CT device that can continuously obtain two-dimensional distribution at 0.5ms interval has been developed. However, the device is not suitable for an industrial powder-particle pipeline because X-ray CT is very expensive, and needs a license for operation. Recently, capacitance CT with real time visualization has been studied as a technique to visualize solid behaviour in solid-air two-phase flow (Huang et al. 1989; Dyakowski et al. 1999). Capacitance CT arranges a sensor consisting of many electrodes around a circumference of a pipeline to measure the capacitances between the electrodes. The distribution of particle density based on the permittivity distribution on the cross section is obtained from a reconstruction method. However, the images obtained by capacitance CT are blurred because approximate values are resolved by a mathematical ill-posed inverse problem. An image analysis is needed to extract the feature of the blurred image to judge the dominant particles from the image.

Currently, the wavelets transform has started to be used for image analysis instead of Fourier transform in mechanical engineering fields. The merits of the wavelets analysis are to be able to analyse the frequency without erasing the time-space information. Wavelets transform[4)] is roughly classified into two types, which are continuous wavelets transform and discrete wavelets transform (Molet 1982). The continuous wavelets transform has been generally used for time frequency analysis in vibration waves. For example, self-similarity of a jet inner structure (Everson et al. 1990), breakdown of a large eddy and successive branching in a plane jet (Li et al. 1995), decomposition of Reynolds stress in a jet (Gordeyev et al. 1995), and multiple acoustic modes and shear layer instability (Walker et al. 1995) were investigated. On the other hand, the discrete wavelets transform has been mainly used for picture image processing. The analysis enables the user to decompose and compose picture images quantitatively because of the orthonormal transform. Saito applied this idea to analysing electromagnetic waves (Saito, 1996). Some of the authors applied this idea to the analysis of jet images (Li et al.,1999). Usually, two-dimensional wavelets transform have been used to obtain the two dimensional original image.

The originality of this paper lies in applying three dimensional discrete wavelets transform to three-dimensional capacitance CT images consisting of two dimensional space and time to extract the particle pattern feature in a pseudo choking state and non-choking state. In this study, particle capacitances downstream of a bend pipe are measured to re-construct the particle density fluctuation images with two dimensional space and time. The images are transformed by three-dimensional discrete wavelets to extract the dominant space-time particle levels in a pseudo choking state and non-choking state.

2 3D DISCRETE WAVELETS TRANSFORM

Three-dimensional wavelets spectrum $\mathbf{S}_{tyx}$ is obtained by

$$\mathbf{S}_{tyx} = [\mathbf{W}_t[\mathbf{W}_y[\mathbf{W}_x\mathbf{E}_{xyt}]^T]^T]^T \tag{1}$$

Where, $\mathbf{E}_{xyt}$ is a three dimensional original image consisting of NxxNyxNt pixels. Nx, Ny and Nt are pixels numbers in *x*, *y* (space axis) and *t* (time axis) directions, respectively, $\mathbf{W}_x$, $\mathbf{W}_y$ and $\mathbf{W}_t$ are the analyzing wavelets matrices consisting of NxxNx pixels, NyxNy pixels and NtxNt pixels, respectively. The transpose matrices are defined by

$$[\mathbf{E}_{xyt}]^T = \mathbf{E}_{txy} \quad [\mathbf{E}_{txy}]^T = \mathbf{E}_{ytx} \quad [\mathbf{E}_{ytx}]^T = \mathbf{E}_{xyt} \tag{2}$$

Therefore, the wavelets spectrum $\mathbf{S}_{tyx}$ is composed of NtxNyxNx pixels. The inverse three dimensional wavelets transform of Eq. (1) is expressed by

$$\mathbf{E}_{xyt} = [\mathbf{W}_x[\mathbf{W}_y[\mathbf{W}_t\,\mathbf{S}_{tyx}]^T]^T]^T \tag{3}$$

In the case of Daubechies orthonormal functions of 2nd order for the analyzing wavelets, and the original image data consisting of Nx=Ny=Nt=32, the original image can be decomposed to each frequency level; namely,

$$\mathbf{E}_{xyt} = \mathbf{E}_0 + \mathbf{E}_1 + \mathbf{E}_2 + \mathbf{E}_3 + \mathbf{E}_4 + \mathbf{E}_5$$

$$\mathbf{E}_0 = [\mathbf{W}_x[\mathbf{W}_y[\mathbf{W}_t\mathbf{S}_0]^T]^T]^T \quad \mathbf{E}_1 = [\mathbf{W}_x[\mathbf{W}_y[\mathbf{W}_t\mathbf{S}_1]^T]^T]^T \quad \mathbf{E}_2 = [\mathbf{W}_x[\mathbf{W}_y[\mathbf{W}_t\mathbf{S}_2]^T]^T]^T$$

$$\mathbf{E}_3 = [\mathbf{W}_x[\mathbf{W}_y[\mathbf{W}_t\mathbf{S}_3]^T]^T]^T \quad \mathbf{E}_4 = [\mathbf{W}_x[\mathbf{W}_y[\mathbf{W}_t\mathbf{S}_4]^T]^T]^T \quad \mathbf{E}_5 = [\mathbf{W}_x[\mathbf{W}_y[\mathbf{W}_t\mathbf{S}_5]^T]^T]^T \tag{4}$$

Where, $\mathbf{S}_0$ is the lowest frequency spectrum, and $\mathbf{S}_5$ is the highest frequency spectrum. Therefore, the image inversely transformed from $\mathbf{S}_0$: $\mathbf{E}_0$ indicates the particle two-dimensional space distribution with the lowest time frequency, which is called time level 0. Therefore, the time level 0 indicates time mean space distribution. On the other hand, the image inversely transformed from $\mathbf{S}_5$: $\mathbf{E}_5$ indicates the two-dimensional space distribution with the highest time frequency, which is called time level 5. Therefore, the time level 5 indicates the most time-fluctuated space distribution. The relation between wavelet levels and the representative space frequencies from the absolute values by Fourier transform is shown in Table 1 in the case of the time interval Δt=10ms. The representative time frequency means the frequency indicating the highest value in the band of the wavelet level. The each level operates a kind of band pass filter.

From Eqs.(1) and (3), the space multiresolution at a specific time wavelet level can be calculated. The two dimensional space image at the specific time wavelet level: $\mathbf{E}_S$ (S=1,2,....5) consisting of Nx x Ny pixels is transformed to the space spectrum, and can be decomposed to the space multiresolution,

$$\mathbf{S}_S = \mathbf{W}_y[\mathbf{W}_x\mathbf{E}_S]^T]^T \tag{5}$$

$$\mathbf{E}_S = \mathbf{Es}_0 + \mathbf{Es}_1 + \mathbf{Es}_2 + \mathbf{Es}_3 + \mathbf{Es}_4 + \mathbf{Es}_5$$

$$\mathbf{Es}_0 = [\mathbf{W}_x[\mathbf{W}_y\mathbf{S}_{S0}]^T]^T \quad \mathbf{Es}_1 = [\mathbf{W}_x[\mathbf{W}_y\mathbf{S}_{S1}]^T]^T \quad \mathbf{Es}_2 = [\mathbf{W}_x[\mathbf{W}_y\mathbf{S}_{S2}]^T]^T$$

$$\mathbf{Es}_3 = [\mathbf{W}_x[\mathbf{W}_y\mathbf{S}_{S3}]^T]^T \quad \mathbf{Es}_4 = [\mathbf{W}_x[\mathbf{W}_y\mathbf{S}_{S4}]^T]^T \quad \mathbf{Es}_5 = [\mathbf{W}_x[\mathbf{W}_y\mathbf{S}_{S5}]^T]^T \tag{6}$$

Where, $\mathbf{S}_{S0}$ is the lowest space frequency spectrum, and $\mathbf{S}_{S5}$ is the highest space frequency spectrum. Therefore, the image inversely transformed from $\mathbf{S}_{S0}$: $\mathbf{E}_{S0}$ indicates the two-dimensional space frequency with the lowest space resolution at the specific time wavelet level, which is called space level 0. Therefore, the space level 0 indicates space mean distribution. The relation between wavelet levels and the representative space frequencies from the absolute values by Fourier transform is shown in Table 1 in the case of one pixel length 1.53 mm.

	Time frequency		Space frequency	
Level	Time frequency [Hz]	Time Wave length [sec]	Space frequency [mm^{-1}]	Space Wave length [mm]
0	3.13	3.19×10^{-1}	2.04×10^{-2}	4.90x10
1	6.25	1.60×10^{-1}	4.08×10^{-2}	2.45x10
2	9.38	1.07×10^{-1}	6.12×10^{-2}	1.63x10
3	1.25x10	8.00×10^{-2}	8.16×10^{-2}	1.23x10
4	2.19x10	4.56×10^{-2}	1.43×10^{-1}	6.99
5	5.00x10	2.00×10^{-2}	3.27×10^{-1}	3.06

Table 1. Relation Between Wavelet Levels and Representative Frequency

3 PRINCIPLE OF CAPACITANCE TOMOGRAPHY

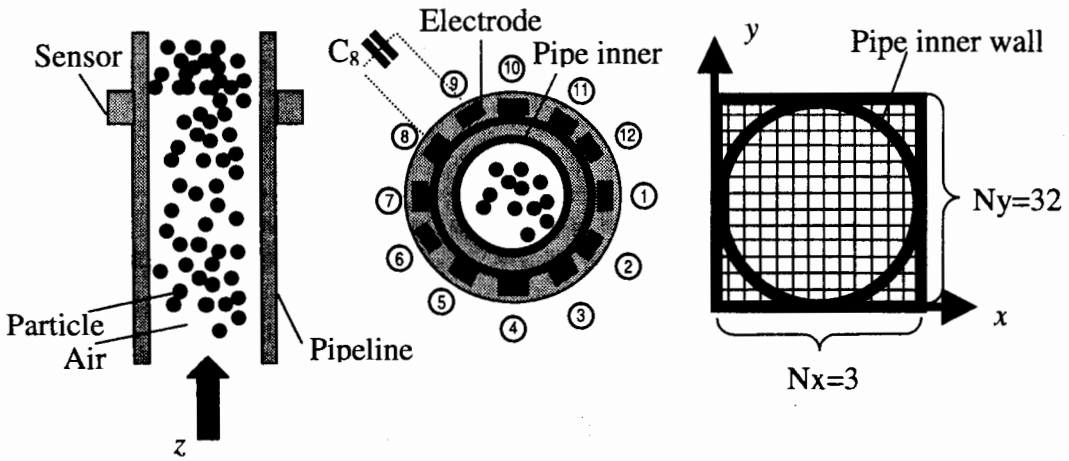

Figure 1: Overview Of Capacitance Tomography and Its Space Resolution

The capacitance CT sensor is set up on the circumference of a pipeline as shown in Figs. 1 (A) and (B). Insulation materials separate the 12 electrodes in the sensor. The relation between capacitance and permittivity in the static electric field is expressed by

$$C_{i,j} = -\frac{\varepsilon_0}{V_c}\oint_{r\subseteq\Gamma_j}\varepsilon(\mathbf{r})\nabla V_i(\mathbf{r})\bullet d\mathbf{r} \tag{7}$$

Where, i is the standard electrode number which is from 1 to 11, and j is the reference electrode number which is from i+1 to 12. C_{ij} is the capacitance between the standard electrode i and the reference electrode j. ε_0 is the vacuum permittivity of air, $\varepsilon(\mathbf{r})$ is the permittivity distribution on the cross section. $\mathbf{r}$ is a position vector on the cross section. V_c is a voltage to the i electrode. Γ_j is an area affected by the electric line of force. $V_i(\mathbf{r})$ is the potential distribution on the cross section between i and j electrodes. Because $V_i(\mathbf{r})$ is unknown in Eq.(7), Laplace equation:

$$\nabla\bullet[\varepsilon(\mathbf{r})\nabla V(\mathbf{r})] = 0 \tag{8}$$

is assumed on the cross section. $V(\mathbf{r})$ is obtained from the discretized Eq.(8). The matrix expression in Eq.(7) showing the relation between the capacitance matrix **C** and the permittivity distributions **E** is

$$\mathbf{C} = \mathbf{S_e}\mathbf{E} \tag{9}$$

Where, the sensitivity map matrix $\mathbf{S_e}$ consists of the known values of ε_0, V_c and $\nabla V_i(\mathbf{r})$ in Eq.(7). In other words, capacitance CT has a method to obtain the permittivity distribution of the particles **E** on

the cross section from both known sensitivity map matrix $\mathbf{S_e}$ and measured capacitance matrix **C**. In the case of 12 electrodes, the sensitivity map $\mathbf{S_e}$ is a 66×1024 matrix in Eq.(9), the capacitance matrix **C** expresses a 66×1 matrix, and the permittivity distribution matrix **E** is a 1024×1 matrix in the case that the pipeline cross section is divided with 32×32 = 1024 square mesh. The mathematical method to obtain the permittivity matrix **E** from the capacitance matrix **C** and the sensitivity map matrix **Se** are ill posed inverse problem because the inverse matrix $\mathbf{S_e}^{-1}$ does not exist. The image is re-constructed by the back projection method.

4 EXPERIMENTS

4.1 Experimental Equipment, Conditions and Method

The experimental equipment is composed of a feeder tank, a pipeline of 49.0 mm internal diameter, a receiver tank and a roots blower as shown in Fig.2. The CT sensor with 12 electrodes was arranged around the pipe circumference downstream of the pipe bend. A 5 cm long pseudo choking part at a point 1 m from the bottom of the vertical pipe is installed to observe the particle behaviour near choking. Clay is attached inside the pipeline at pseudo choking part. The pseudo choking part has clay at ratios of 0 and 3/4 of the pipe cross-section area as shown in Fig.3. Therefore, the open area ratios A are 1.0 and 0.195. A=1.0 means a non-choking state. The air suction volume was 0.019 m3/s; the particle was supplied at 284.8 g/s. The mean air velocity in the pipeline calculated from the air volume was 9.68 m/s, Reynolds number was 3.22×10^4, and the solid air ratio was 12.46. The particles were polyethylene pellets, which were almost spherical with 3.26 mm diameter and 910 kg/m^3 density. The time interval to acquire one frame is Δt= 10.0 ms. The 32 consecutive frames for 320.0 ms are picked up to be analysed in the next section among the total reconstructed frames for 60.0 second.

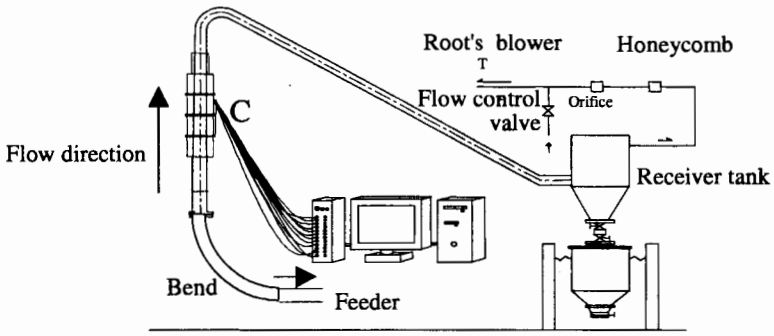

Figure 2: Experimental Equipment

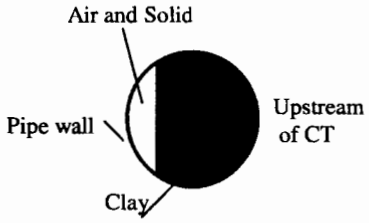

Figure 3: Pseudo Choking Part

In this study, the permittivity matrix **E**, which indicates the particle two-dimensional space distribution at a time, is normalized with the maximum value 1.0 and minimum value 0.0 by a calibration. The maximum value corresponds to particles occupying the whole cross-section. The minimum value corresponds to air occupying the whole cross-section. One image pixel is 1.53×1.53 mm^2 because the inside cross-section of 49.0 mm is divided with 32×32 image pixels. When a particle core passes through the measurement section, the diameter of one particle holds 2.13 image pixels because the particle diameter is 3.26mm. Accurately, this sensor obtains the particle density fluctuation distribution in a cell Δz × one image pixel for Δt. The flow direction length of the sensor Δz = 63.0 mm. The particle distance for Δt is about $v_p \Delta t$ = 17.6 mm (the particle mean velocity v_p is assumed to be the mean air velocity).

4.2 Experimental Results

The reconstructed three dimensional image obtained by the CT: $\mathbf{E_{xyt}}$ is re-calculated to the density fluctuation image $\mathbf{E'_{xyt}}$ by the root mean square,

$$\mathbf{E'}_{xyt} = (\mathbf{E}_{xyt} - \bar{\mathbf{E}}) / \mathbf{E}_{RMS} \qquad (10)$$

Where, $\mathbf{E'}_{xyt}$ is the distribution of the particle density fluctuation at x, y, and t point in a cell Δz × one image pixel for Δt. The root mean square and the time-space mean value is calculated by

$$\mathbf{E}_{RMS} = \frac{1}{\mathrm{Nt\ Ny\ Nx}} \sum_{t=1}^{Nt} \sum_{y=1}^{Ny} \sum_{x=1}^{Nx} \sqrt{\left(\mathbf{E}_{xyt} - \overline{\mathbf{E}}\right)^2} \qquad \overline{\mathbf{E}} = \frac{1}{\mathrm{Nt\ Ny\ Nx}} \sum_{t=1}^{Nt} \sum_{y=1}^{Ny} \sum_{x=1}^{Nx} \mathbf{E}_{xyt} \tag{11}$$

The representative fluctuation images $\mathbf{E'}_{xyt}$ at $4\Delta t$, $12\Delta t$, $20\Delta t$ and $28\Delta t$ (Δt=10ms) in the non-choking state and at $7\Delta t$, $15\Delta t$, $23\Delta t$ and $31\Delta t$ in the pseudo choking state from the experimental results are shown in Fig.4. The image pixel, where any particles do not exist, is black. As the particle density fluctuation on an image pixel becomes high, the image pixel changes into white with 10 stages in the colour bar. The highest and lowest values are different in each state. On the whole, the distribution of particle density fluctuation is qualitatively visualized. In the case of the non-choking state, the particles are slightly partial to the outside of the pipeline because of the centrifugal force caused by the bend. In the choking state, the particles are largely partial to the outside. Also, it is realized that images have steady and unsteady components in time. For example, points A and C are steady positions in time because the points at every frame keep the particle density fluctuation; however, points B and D are unsteady positions because the every frame except does not exist the particle density fluctuation.

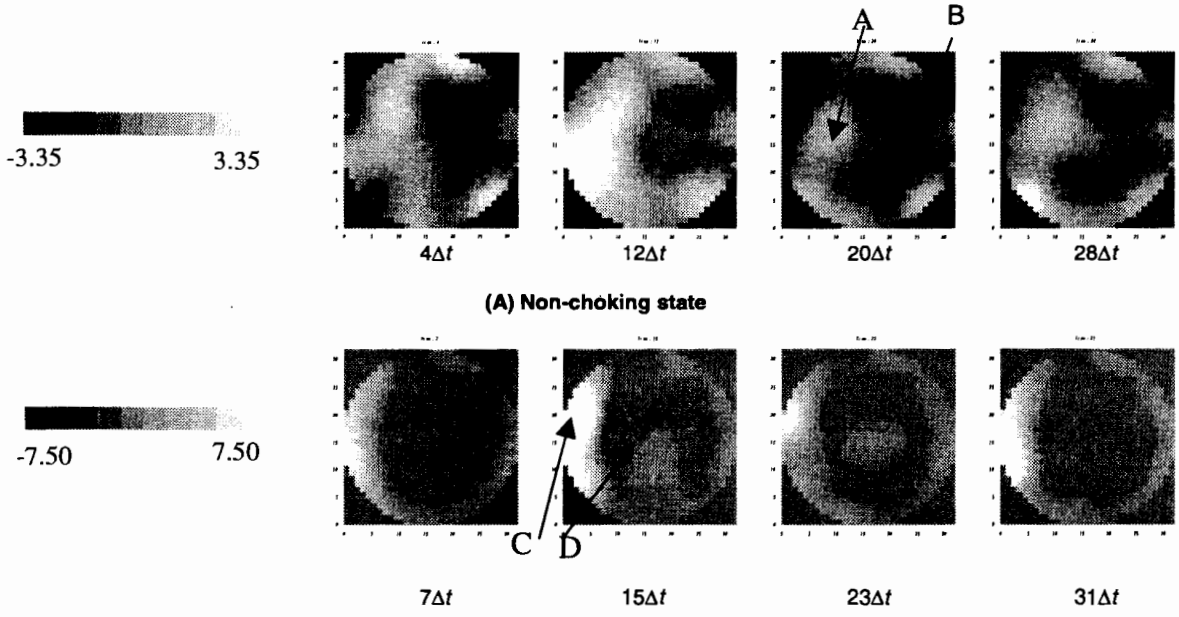

Figure 4. Tomography Image of Particle Density Fluctuation

5 ANALYSIS AND DISCUSSION

5.1 Wavelets Multiresolution to Time

Firstly, the time multiresolution of the particle density fluctuation is calculated by Eq.(4) to decompose the three dimensional original image from time level 0 to time level 5. The time level 0 indicates the steady two-dimensional space distribution of the particle density fluctuation during the time. The time level 5 indicates the unsteadiest distribution of particle density fluctuation during the time. To simplify the unsteady behaviour, the multiresolution is classified into the two groups that are level 0 and over level 1 by

$$\mathbf{E'}_{xyt} = \mathbf{E'}_S + \mathbf{E'}_U \qquad \mathbf{E'}_S = \mathbf{E'}_0 \qquad \mathbf{E'}_U = \mathbf{E'}_1 + \mathbf{E'}_2 + \mathbf{E'}_3 + \mathbf{E'}_4 + \mathbf{E'}_5 \tag{12}$$

The steady particle density fluctuation $\mathbf{E'}_S$ is the same as the mean distribution calculated from

$$\overline{\mathbf{E}_{xy}}' = \frac{1}{Nt} \sum_{t=1}^{Nt} \mathbf{E'}_{xyt} \tag{13}$$

in the case of Daubechies function of 2nd order as the wavelets analysing function. Figs. 5 and 6 are the particle density fluctuation image decomposed by the wavelets multiresolution in the non-choking state and the choking state respectively. (A) shows the steady image: $\mathbf{E'_S}$, (B) shows the representative unsteady image: $\mathbf{E'_U}$. The summation between the steady image $\mathbf{E'_S}$ and the unsteady image at a time $\mathbf{E'_U}$ completely recovers the original image $\mathbf{E'_{xyt}}$ in Fig. 4 because of the orthonormal transform. Moreover, to clarify the unstable image in detail, time level 5 images $\mathbf{E'_5}$ are representatively shown in (C). From Figs. 5(B) and 6(B), it is realized that the fluctuation images at $20\Delta t$ in the non-choking state and at $23\Delta t$ in the choking state have the negative fluctuation from the mean image on the whole. Moreover, for example, the negative E point on the unsteady image at $12\Delta t$ in the choking state is more affected by the time level 5 image (F point) than the steady image (G point). The positive H point on the unsteady image at $15\Delta t$ in the choking state is more affected by both steady image (J point) and time level 5 image (I point). Above all, the decomposed image by 3D wavelets contributes to realizing the detail space distribution to the various time frequencies.

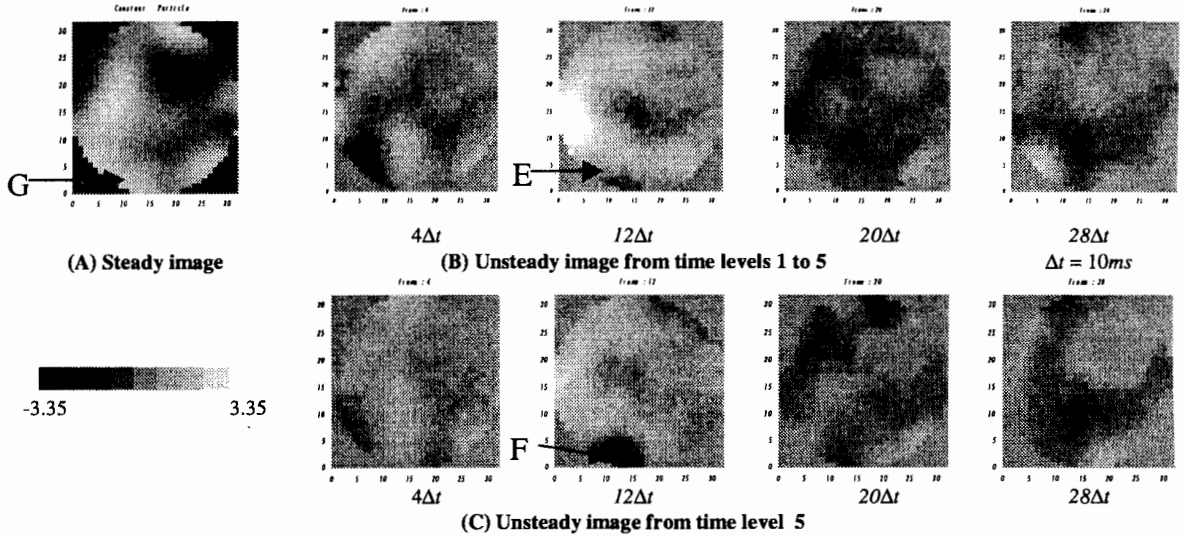

Figure 5. Steady and Unsteady Particle Density Fluctuation Images in Non-Choking State

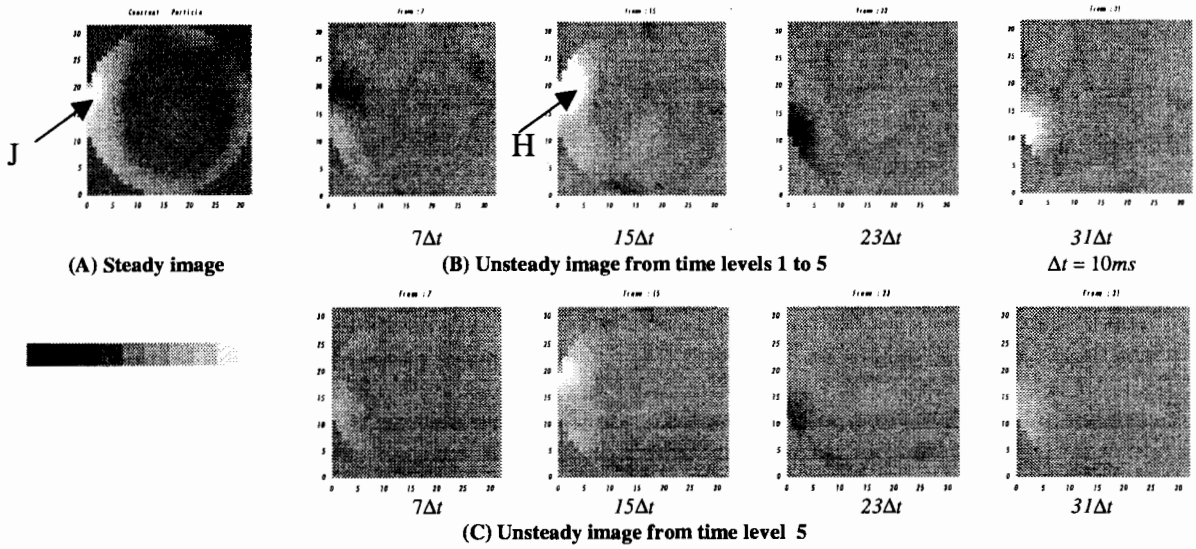

Figure 6. Steady and Unsteady Particle Density Fluctuation Images in Choking State

The dynamic range subtracting the minimum value from the highest value at a time wavelet level is shown in Fig. 7. It plunges into the bottom at time level 1, and it increases toward time level 5. In the non-choking state, time levels 4 and 5 with high time frequency are larger in terms of the time fluctuation than time level 0, which indicates the time mean value; the dynamic range of the steady particle density fluctuation is 3.58. In the choking state, only level 5 is larger than level 0 that is 8.34. From this figure, it is realized that the dynamic range in the non-choking state is much larger than that in the choking state, and that the time dominant levels of the fluctuation are levels 4 and 5 in the non-

choking state; however, it is level 5 in the non-choking state. It means the choking state fluctuates the particles largely to result in shifting the dominant level to the higher level. The dynamic ranges of the steady and unsteady particles in time series are calculated in Fig. 8. This figure reveals two peaks at 11Δt ms and 32Δt ms in the non-choking state, and at 15Δt ms and 31Δt ms in the choking state. These times show the highest fluctuations of the particle density fluctuation. In detail, the unsteady particle density fluctuations at the dominant time levels 4 and 5 are shown in Fig. 9. In the non-choking state (A), the first peak is significantly caused by the level 5, which means the highest time frequency. However, the second peak is caused by, not only time level 5 but also, time level 4. In the choking state (B), both peaks are mainly affected by time level 5; however, time level 4 causes the peaks even though the dynamic range is lower than time level 0 in Fig. 7. Above all, the time dominant level and its time can be extracted from the wavelet multiresolution clearly.

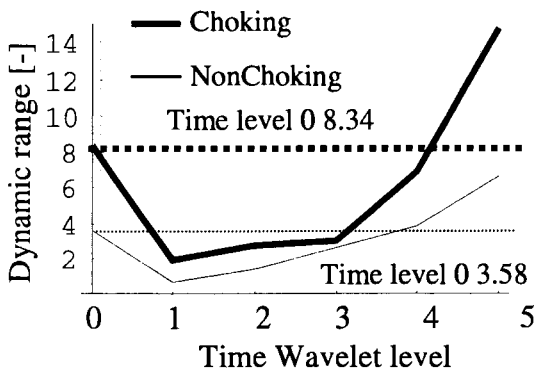

Figure 7. Dynamic Range at Time Level

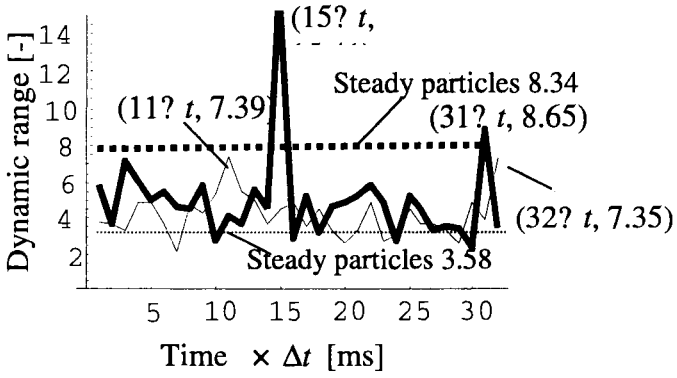

Figure 8. Dynamic Range of Steady & Unsteady Particles

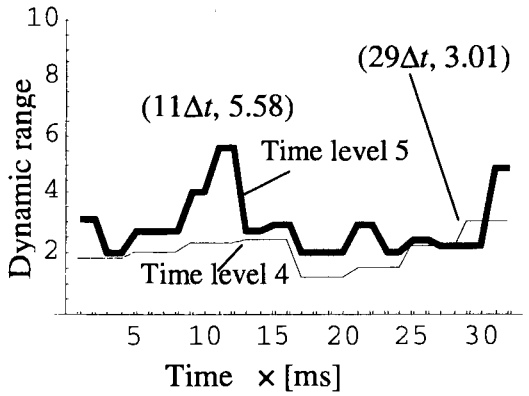

(A) Time Levels 4 and 5 in Non-Choking Sate

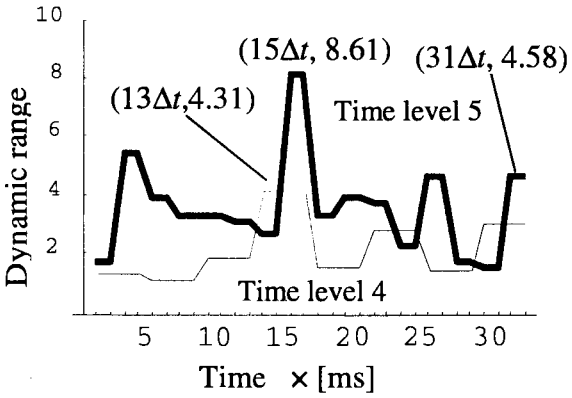

(B) Time Levels 4 and 5 in Choking State

Figure 9. Dynamic Range of Steady and Unsteady Particle Density Fluctuation to Time

5.2 Wavelets Multiresolution to Space

The images of the unsteady particle density fluctuations are decomposed to the space multiresolution, based on the time dominant levels 4 and 5 using Eq.(6), in order to calculate the dynamic range at the dominant space wavelet level. Figs. 10(A) and (B) are the relation between the time and the space wavelet levels at the time wavelet levels 4 and 5 in the choking state and the non-choking state, respectively. In the non-choking state, Fig. 10(A-1) of the time wavelet level 4 indicates two relatively high peaks which are at space level 5 11Δt ms (point P), and at space level 3 29Δt ms (point Q). It means the particle density fluctuation with high space frequency, which is a small particle lump, passes through the sensor cross-section at 11Δt ms; however, the particle density fluctuation with middle space frequency, which is middle particle lump, passes through the sensor cross-section at 29Δt ms. Fig. 10(A-2) of the time wavelet level 5 indicates two peaks which are at the space level 5 11Δt ms (point R), and at the space level 3 32Δt ms (point S). It means the small particle lump passes through at 11Δt ms; however, the middle particle lump, passes at 32Δt ms. In the case of the choking state, two peaks are visible at the space level 5 15Δt ms (point T) and at space level 5 15Δt ms (point

U) as shown in Figs. 10(B-1) and (B-2). However, point U at the time level 5 is much larger than point T at the time level 4. It means the particle density fluctuation with high space frequency passes through the sensor cross-section at the time. From these figures, the non-choking state has the peaks the lower space level. However, the choking state has the peaks at the only high space level 5 because the dominant fast time fluctuation (time level 5) breaks the middle particle lump (space level 3) to reach the highest space level 5 in the choking state. However, from Figs. 7 and 9, the suitable time fluctuation (time level 4) maintains the middle particle lump relatively in the non-choking state. Fig. 11 shows the time-space image with the highest dynamic range of the particle density fluctuation at points P, Q, R, S and U. The image at point T is omitted. Form these figures, this technique can recognize the space distribution of the particle density fluctuation on the dominant time-space levels simultaneously.

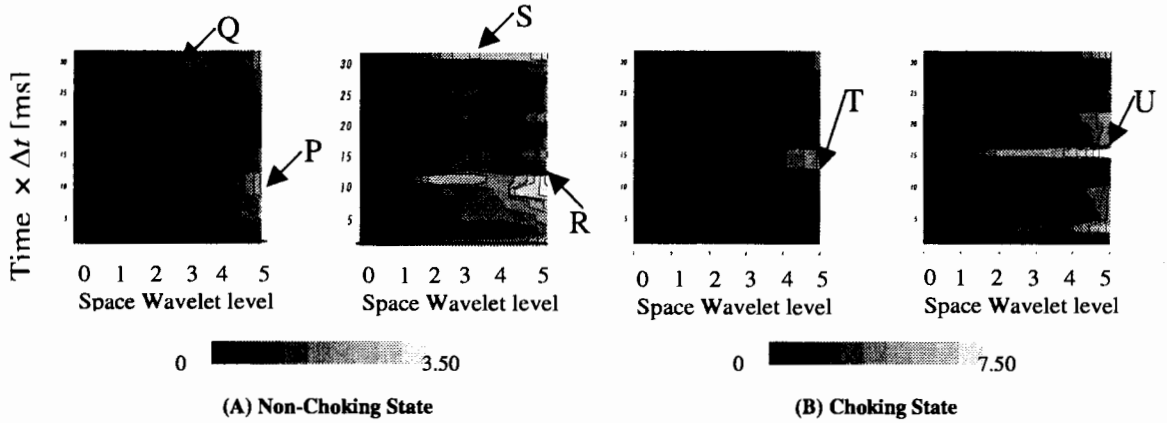

Figure 10. Dynamic Range of Steady and Unsteady Particles to Space

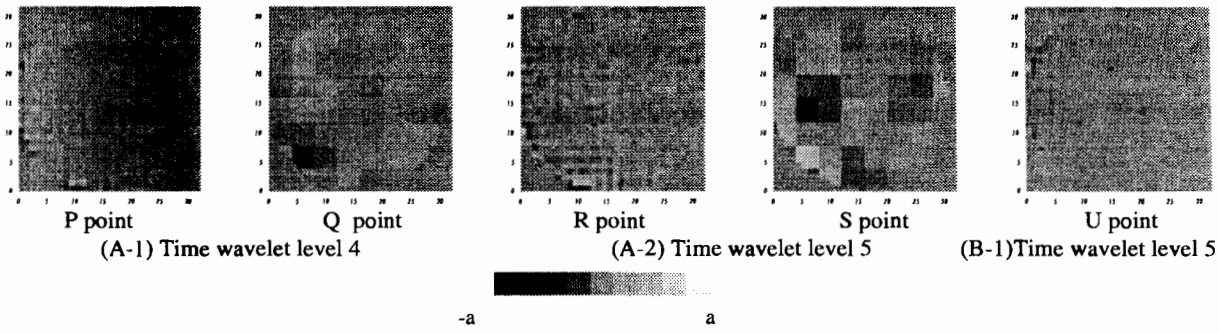

Figure 11. Time-Space Dominant Image of Particle Density Fluctuation

6 CONCLUSIONS

A concept to extract dominant particle levels in time-space on a pipeline cross section has been launched using capacitance-computed tomography and three-dimensional discrete wavelets transform to analyse the particle density fluctuation in a non-choking state and a pseudo choking state. The follows are made clear.

1) This concept enables the user to realize the time and position when and where the particle density fluctuation with time-space dominant levels passes through the pipeline simultaneously.

2) The formation of the particle density fluctuation has several types in terms of time and space frequency in the non-choking state. In detail, the particle density fluctuation with time and space wavelet levels 5, which indicates the highest time-space frequency level, passes through the pipeline in a time; however, the particles with the time wavelet level 5 and space wavelet level 3 pass through the pipeline in the other time.

3) The choking state has the peaks at the only highest space level 5 because the dominant fast time fluctuation (time level 5) breaks the middle particle lump (space level 3) to reach the highest space level 5.

This study is supported financially by Japan Science and Technology Corporation. The authors greatly wish to thank Mr. Malcolm Byars of PTL in UK and Mr. Masaho Nagoshi of Kanomax Japan Inc.

7 REFERENCES

DYAKOWSKI,T., LUKE,S.P., OSTROWSKI,K.L. and WILLIAMS,R.A.(1999) On-Line Monitoring of Dense Phase Flow Using Real Time Dielectric Imaging, *Powder technol*, 104,287-295

EVERSON,R. and SIROVICH,L. (1990) Wavelets Analysis to the Turbulence Jet, *Phys.Lett.*, Vol.145 No.6, pp314-322

GORDEYEV,S.V. and THOMAS,F.O. (1995) Measurement of Reynolds Stress Reversal in a Planar Jet by Means of a Wavelets Decomposition, *Turbulent Flows ASME*. FED-Vol.208. pp.49-54

HUANG,S.M., PLASKOWSKI,A.B., XIE,C.G., and BECK,M.S. (1989) Tomographic Imaging of Two-Component Flow Using Capacitance Sensors, *J.Phys, E: Sci, Intrrum*, 22 , pp173-177

LI,H. and NOZAKI,T. (1995) Wavelets Analysis for the Plane Turbulence, *JSME International Journal Fluids and Thermal Engineering*, Vol.38, No.4 pp525-531

LI,H, TAKEI, M., OCHI, M., SAITO, Y. and HORII, K. (1999) Application of Two-dimensional Orthogonal Wavelets to Multiresolution Image Analysis of a Turbulent Jet, *Transactions of the Japan Society for Aeronautical and Space Sciences*, Vol.42, No.137, pp120-127

MOLET,F. (1982) Wavelets Propagation and Sampling Theory, *Geophysics*, Vol.47,pp203-236

ROSENFELD,A. and KAK,A.C. (1982) Digital Picture Processing, Academic Press

SAITO,Y. (1996) Wavelets Analysis for Computational Electromagnetics, (in Japanese), *Trans. IEE of Japan,* Vol. 116A, No10, pp833-839

WALKER,S.H., GORDEYEV,S.V. and THOMAS,F.O. (1995) A Wavelets Transform Analysis Applied to Unsteady Jet Screech Resonance, *High speed jet flow ASME*. FED-Vol.214.pp103-108.